Journal of Applied Physics

RESEARCH ARTICLE | FEBRUARY 19 2026

AlN-on-sapphire microdisk resonators for precise on-chip temperature sensing

D. O. Armstrong ; J. K. Cannon ; O. Kiely ; S. Ibrahim ; H. B. Yağcı ; T. Peach ; P. Wong ; J. P. Hadden ; A. J. Bennett

J. Appl. Phys. 139, 073104 (2026)
https://doi.org/10.1063/5.0313161

Journal of Applied Physics ARTICLE pubs.aip.org/aip/jap

AlN-on-sapphire microdisk resonators for precise on-chip temperature sensing

Cite as: J. Appl. Phys. **139**, 073104 (2026); doi: 10.1063/5.0313161
Submitted: 20 November 2025 · Accepted: 31 January 2026 ·
Published Online: 19 February 2026

D. O. Armstrong,[1,a] J. K. Cannon,[1,a] O. Kiely,[1,a] S. Ibrahim,[1] H. B. Yağcı,[1,a] T. Peach,[2] P. Wong,[2] J. P. Hadden,[1,a] and A. J. Bennett[1,a),b)]

AFFILIATIONS

[1]School of Engineering, Cardiff University, Queen's Buildings, The Parade, Cardiff CF24 3AA, United Kingdom
[2]Institute for Compound Semiconductors, Translational Research Hub, Maindy Road, Cardiff CF24 4HQ, United Kingdom

[a)]**Also at:** Translational Research Hub, Maindy Road, Cardiff CF24 4HQ, United Kingdom.
[b)]**Author to whom correspondence should be addressed:** bennetta19@cardiff.ac.uk

ABSTRACT

Photonic integrated circuit sensors can be used for precise sensing of the environment, offering the advantage of integration with fiber networks for remote and multiplexed sensor arrays. In this work, we examine the performance of aluminum nitride on sapphire microdisk mode resonators in an all-pass configuration. We discuss their potential as on-chip temperature sensors under *fixed-frequency* and *frequency-scanning* modes, demonstrating the latter can measure a 1 K temperature change with an uncertainty of ±5.1 mK over a temperature range of 25–55 °C.

I. INTRODUCTION

Aluminum nitride (AlN) is a CMOS-compatible, wide-bandgap semiconductor[1] with a transparency window spanning the ultraviolet to infrared.[2] This property allows photonic devices to operate across a wide range of wavelengths. Boasting second- and third-order optical nonlinearity,[3] AlN is a promising platform for second harmonic generation,[4,5] sum/difference generation,[6] and four-wave mixing.[7] AlN's piezoelectrical properties make it attractive for optical-mechanical coupling. The advanced epitaxy, manufacturing, and materials science of AlN have been driven by commercial applications inside lighting, electronics, and surface acoustic wave filters, which means it is widely available on large wafers. Additionally, AlN and sapphire have bulk properties that make them a desirable platform for applications in harsh environments such as a high melting point (≈ 2800 K for AlN[8]), chemical resistance,[9] and radiation tolerance.[10,11]

Most studies of AlN as a platform for integrated photonics have used microring resonators (MRRs) inside silica or supported on sapphire substrates,[2–5,7] where a closed-loop single mode waveguide is evanescently coupled to a bus waveguide. An alternative design of resonator uses whispering gallery modes, which occur when light is confined to the edges of a circular disk of dielectric[12,13] called a microdisk resonator (MDR). The multimodal nature of MDRs offers more resonances to track the shift in temperature than their MRR counterparts. This provides more data points to infer the temperature of the resonator, aiding in lowering the measurement uncertainty.

Chip-based resonators can be used as sub-millimeter scale sensors with tolerance to harsh environments. MDRs have been used to realize optical sensors[14,15] and for bio-chemical sample characterization.[10,12,16] Furthermore, changes in temperature affect the bulk material properties of the resonator leading to shifts in positions of resonances. Chip-based temperature sensors can be integrated into arrays that can identify local heating or temperature gradients, mass-produced in semiconductor cleanrooms. Temperature sensing using MRRs has been discussed in silicon,[17–19] silicon nitride,[20,21] and transfer-printed diamond on gallium nitride.[22] These photonic temperature sensors can outperform the Standard Platinum Resistance Thermometers (SPRTs) commonly used in scientific instrumentation,[23,24] which are limited to an accuracy of approximately 10–100 mK.[25,26]

Two methodologies can be followed to probe changes to the environment of a photonic sensor; a *fixed frequency* measurement

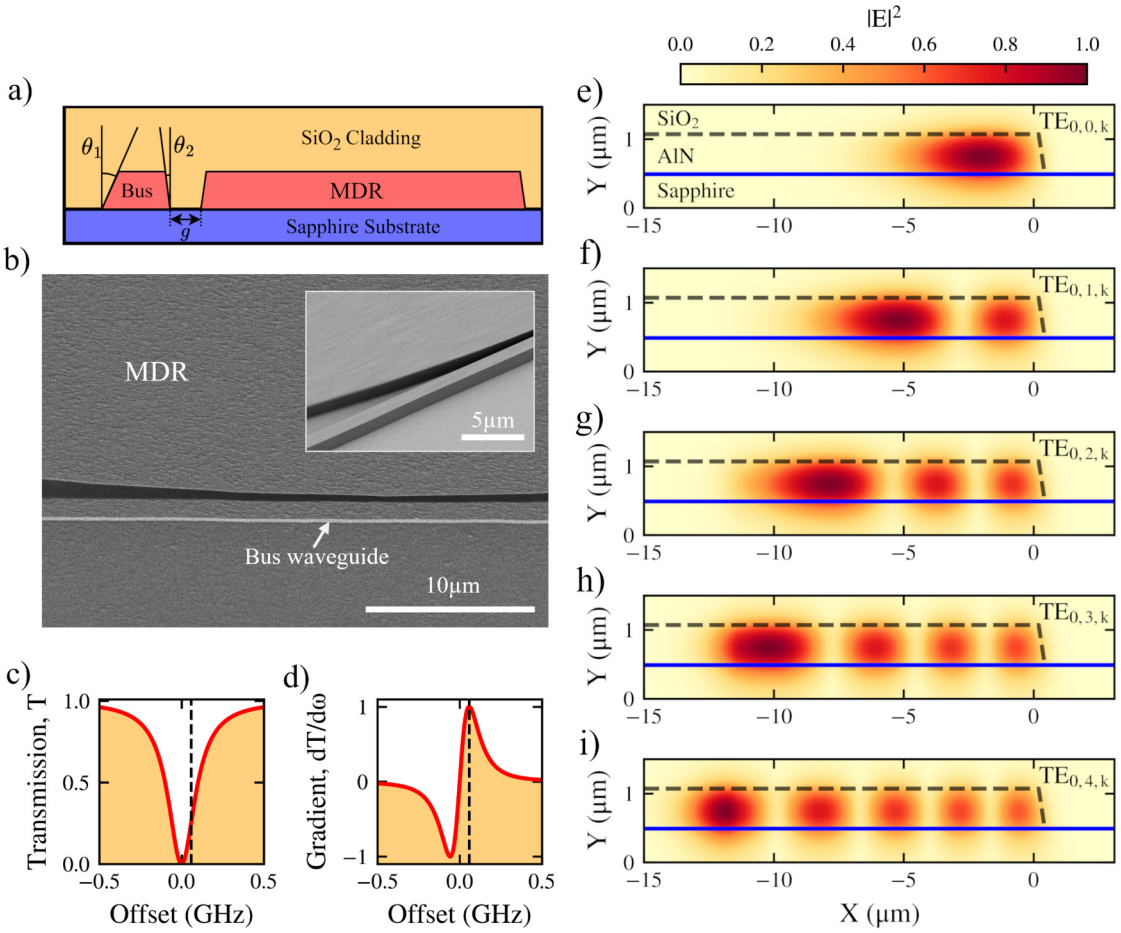

FIG. 1. Diagram of a microdisk resonator. (a) Schematic of the MDR and bus waveguide (not to scale). (b) Scanning electron microscope image of MDR and bus waveguide, and (inset) view at an oblique angle. The top-down SEM image shows the sidewalls as bright regions, from which we infer the angle of the sidewall. (c) Transmission spectrum and (d) its derivative for a typical resonance. (e)–(i) Simulated mode profiles of the $TE_{0,0,k}$ to $TE_{0,4,k}$.

can be made by aligning a laser with the steepest part of the transmission spectrum and monitoring the power as shifts in the resonance central frequency change the intensity. This method allows for high precision sensing albeit over a small range. Alternatively, a *frequency scanning* measurement, where a narrowband laser is swept over one or more resonances, can be employed. In this case, fitting can find the central frequency of the mode with far greater accuracy than the resonance width, but at a cost in readout time. In both cases, it is advantageous to have a high Q cavity and a high extinction of the transmission. Here, we investigate AlN-on-sapphire all-pass MDRs fabricated using electron-beam lithography and dry etching. We characterize devices manufactured from commercially available wafer material at ambient temperature using C-band light. We discuss the optimal device parameters for sensing changes in the local environment and demonstrate a photonic thermometer with accuracy surpassing that of SPRTs, showing this is a promising platform for integrated sensing.

II. MODE STRUCTURE OF MICRODISK RESONATORS

Figure 1(a) shows the design of an MDR coupled to a straight bus waveguide, where the coupling gap, g, controls the coupling between the single mode in the bus and the MDR modes. Angles θ_1 and θ_2 define the verticality of the waveguide sidewalls in regions outside and inside of the coupling region, respectively. Figure 1(b) summarizes the asymmetric sidewall angle showing a SEM image of the coupling region for a fabricated MDR on the same chip, which has not been clad in SiO_2. The transmission spectrum through the system has a Lorentzian form for a single mode, where the visibility of the transmission spectrum is determined by the balance between coupling strength and MDR loss. At critical coupling, when loss per round trip is matched to the bus-MDR outcoupling, the visibility of the transmission spectrum is maximized as illustrated in Fig. 1(c). This line shape has a maximum gradient at an offset of

$\pm\Gamma/\sqrt{3}$ from the central frequency, where Γ is the half-width at half maximum of the resonance, shown as a dotted line in Fig. 1(d). This is the optimum offset for use in a fixed-frequency sensing mode.

Finite difference element simulations using Lumerical are shown in Figs. 1(e)–1(i), depicting the mode profiles of the first five TE modes in a radial segment of the MDR with a bending radius of 200 μm. Modes identified in the resonator are denoted $TE_{i,j,k}$ where conventionally $i+1$ is the number of antinodes in the electric field intensity along the growth direction, $j+1$ is the number of antinodes along the radial direction, and $k+1$ is the number of antinodes around the azimuth. Plots of the $TE_{0,j,k}$ modes for $j = 0, 1, 2, 3, 4$ are shown in Fig. 1(e). The group index of the $TE_{0,0,k}$ mode is $n_g = 2.051$ at 1550 nm, from which we can infer the free-spectral range (*FSR*) in frequency space,[27]

$$FSR = \frac{c}{n_g \times L} = 116.3\,\text{GHz}, \tag{1}$$

where L is taken to be the MDR circumference.

The spectrum of an MDR that is close to critically coupled for $TE_{0,0,k}$ consists of many resonances per *FSR*. This is because although higher-order ($j > 0$) modes have reduced coupling to the bus waveguide, they also have reduced round-trip loss as a result of reduced overlap with the etched sidewalls of the MDR. Thus, these modes are also visible in the transmission spectrum. The table shows the calculated group index of the five modes simulated in Fig. 1.

For the $TE_{0,1,k}$ mode, with a group index of 2.044, the offset in resonant frequency relative to the $TE_{0,0,k}$ mode, $\delta\nu = -0.655$ THz, corresponds to a shift of $-5.63FSR$ in the resonance frequency. Therefore, we can say that the $j = 1$ mode within the same *FSR* as $TE_{0,0,k}$ will be $TE_{0,1,k+5}$ and it will be offset by $-0.63FSR$. By similar reasoning, each 116.3 GHz of the transmission spectrum will contain at least five jth modes in order of decreasing frequency $TE_{0,0,k}$, $TE_{0,3,k+15}$ at $-0.31FSR$ offset from $TE_{0,0,k}$, $TE_{0,2,k+10}$ at $-0.42FSR$ offset, $TE_{0,4,k+19}$ at $-0.50FSR$ offset, and $TE_{0,1,k+5}$ at $-0.63FSR$ offset (Table I). As we show later, this plethora of high-visibility and high-quality factor transmission resonances confer an advantage in reducing the uncertainty in frequency-scanning temperature measurements.

TABLE I. Simulated group index values for the first five TE modes found in our MDR.

Mode	n_g	$\delta\nu$(THz)	$\frac{\delta\nu}{FSR}$
$TE_{0,0,k}$	2.051	N/A	N/A
$TE_{0,1,k}$	2.044	−0.655	−5.63
$TE_{0,2,k}$	2.038	−1.212	−10.42
$TE_{0,3,k}$	2.032	−1.780	−15.31
$TE_{0,4,k}$	2.027	−2.268	−19.50

III. RESULTS

A. Resonator characterization

The sample is a 600 nm epilayer of AlN-on-sapphire grown by metal organic chemical vapor deposition (MOCVD) on the C-plane. Sample quality is assessed by x-ray diffraction (XRD) with a full width half maximum (FWHM) of 98 arc sec at the [002] peak. The MDR devices were patterned by electron beam lithography with a negative resist, which was transferred to a silica hard-mask, prior to inductively coupled plasma etching (chlorine-argon etch chemistry) of the semiconductor. After removal of the silicon dioxide hard mask, the sample was clad with a 2 μm coating of SiO_2. During a scanning electron microscope (SEM) inspection of the etched structure, it was noted that on sparse areas of the sample the etch achieved a typical sidewall angle of 16°. However, in the vicinity of the coupling gap, the sidewall angle decreases to 8°, depending on g. The variation in sidewall angle was consistently observed across all fabricated devices. Therefore, we conclude that this is a result of the plasma dynamics during dry etching of the semiconductor in a restricted volume. Each MDR has a radius of 200 μm and is coupled to a single mode bus waveguide with a nominal width of 1.2 μm in an "all-pass" configuration,[27] as shown in Fig. 1. As shown in Fig. 2(a), a C-band tunable continuous-wave laser with a linewidth of 100 kHz was used to characterize the device by scanning in steps of 10 MHz. Light was coupled into and out of the bus waveguide with a 1D grating coupler (duty cycle of 62%, pitch of 1.2 μm) via a fiber array with piezo-controlled positioning. TE input polarization was selected using a paddle-style polarization controller.

Figure 2(b) shows the normalized transmission spectrum of the MDR revealing multiple narrow resonances. We observe a repeating pattern with a $FSR \approx 116$ GHz, which is close to that predicted from simulation. Greater intensity is seen at the red end of the spectrum, where the grating couplers are more efficient. Between resonances, there is a low-visibility sinusoidal oscillation (with period ~27 GHz) resulting from a weak Fabry–Pérot cavity formed by backreflections from the grating couplers. The zoom-in of the transmission spectrum shown in Fig. 2(c) shows the multimodal nature of the MDR resonators with five modes resolved within each *FSR*. In the analysis that follows, we focus on the isolated resonances marked with arrows, which result from coupling to the $TE_{0,0,k}$ MDR modes.

By adjusting the distance between the bus waveguide and the MDR, the coupling to the $TE_{0,0,k}$ modes can be tuned. Identical MDR devices with coupling gaps ranging from 100 to 500 nm were fabricated. Figures 2(d) and 2(e) show resonances measured when close to critical coupling, with $g = 150$ nm, and when under-coupled $g = 500$ nm. The average loaded (measured) quality factor Q_L and transmission on resonance were used to calculate the intrinsic quality factor Q_I, which quantifies the resonator's quality in the absence of the bus, using the formula

$$Q_I = \frac{2Q_L}{1 \pm T^{1/2}}, \tag{2}$$

where T is the on-resonance transmission. The summation or subtraction operator in the denominator of Eq. (2) depends on the case of under or over-coupling, respectively.

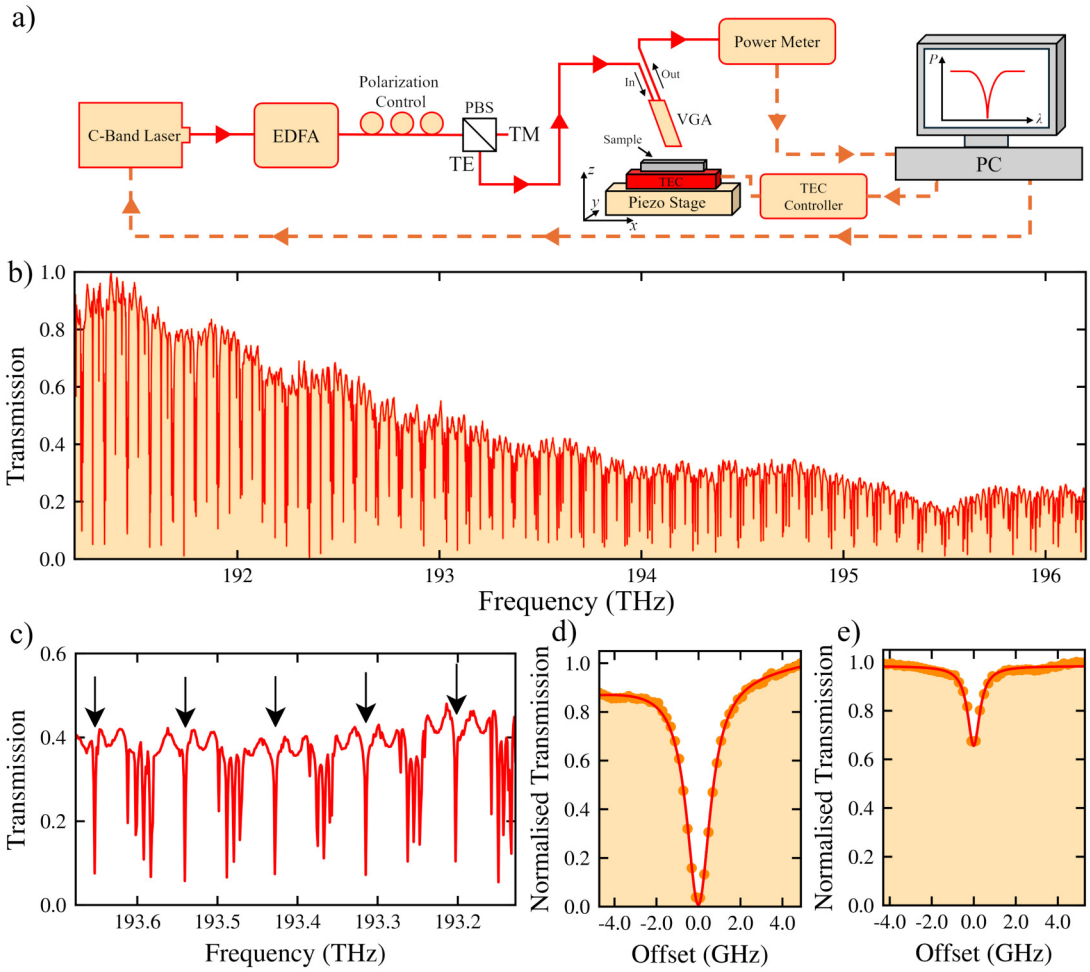

FIG. 2. (a) Schematic illustration of the experimental setup. (b) Transmission spectrum of an AlN microdisk resonator with a coupling gap of 150 nm. (c) Zoomed in view of the same transmission spectrum, with arrows marking the $TE_{0,0,k}$ resonances. (d) Fit to a critically coupled MDR device with $Q_L = 1.40 \times 10^5$ and $Q_I = 2.78 \times 10^5$. (e) Fit to an undercoupled device on the same chip with $Q_L = 2.75 \times 10^5$ and $Q_I = 3.02 \times 10^5$.

Figure 3 shows these values as a function of coupling gap. The mean Q factor was determined from five $TE_{0,0,k}$ resonances [marked with arrows in Fig. 3(b)] using a Lorentzian line shape with a polynomial background. The MDR with $TE_{0,0,k}$ closest to critical coupling had $g = 150$ nm showing an average on-resonance transmission of 0.02. The average values of Q_L and Q_I for the near-critically coupled device were $(136 \pm 3) \times 10^3$ and $(238 \pm 5) \times 10^3$, respectively. These Q factors exceed previous reports of MDRs fabricated in sputtered AlN-on-silica,[28] but fall below the best reported Q factors seen in epitaxial AlN-on-sapphire single mode ring resonators.[29] In future, improvements to the Q factor may be achieved by optimizing the resonator's edge roughness, for example, by improvements to the dry etching process. Some work has reported that initially coating the resonators in oxide by conformal atomic layer deposition[30] and/or post cladding thermal annealing[5,31] may further increase

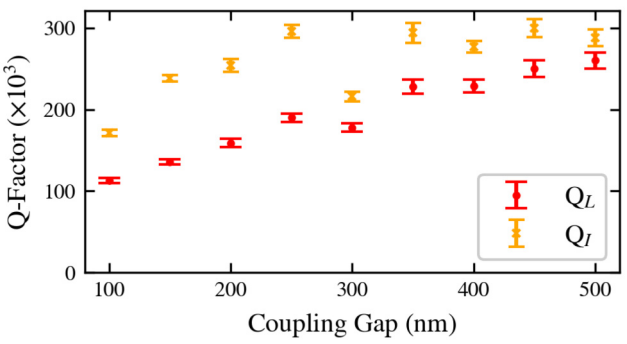

FIG. 3. Loaded (Q_L) and intrinsic (Q_I) Q factors of the $TE_{0,0,k}$ mode for MDR devices with a varying coupling gap, g.

Q. The datapoint at a coupling gap of 300 nm has an anomalously low Q_L as a result of a fabrication defect visible near the MDR edge. In the vicinity of the coupling region, the MDR sidewall angle is expected to decrease. This may be the cause of the change in the intrinsic quality factor observed in Fig. 3 at small gaps.

B. Fixed frequency MDR thermometry

As the resonant frequencies of the MDR devices are sensitive to temperature, they can be used as an on-chip photonic thermometer. A simple sensing mode is to use a narrow single-frequency laser at the steepest part of the transmission spectrum, as illustrated in Figs. 1(c) and 1(d). This occurs at $\nu_{i,j,k} \pm \Gamma/[\sqrt{3}]$, when the transmission dip is a Lorentzian of half-width Γ. Transmitted intensity can be monitored, providing a measurement of small temperature changes over a limited range. It can be shown that the maximum gradient of the transmission spectrum for a resonator, with fixed round-trip loss, is always obtained when the resonator is critically coupled. This gives a maximum visibility of the transmission dip, at a cost of halving the quality factor from its intrinsic value. The gradient of the transmission, T, vs frequency, ν, is

$$\frac{dT}{d\nu} = \frac{2T_0\Gamma^2(\nu - \nu_{i,j,k})}{\left(\Gamma^2 + (\nu - \nu_{i,j,k})^2\right)^2}, \tag{3}$$

where T_0 is the transmission away from the resonance, Γ is the (i, j, k)th mode half-width half maximum (HWHM) $(\nu_{i,j,k}/2Q_{i,j,k})$, and $\nu_{i,j,k}$ is the resonance's central frequency. At the maximum gradient, this becomes

$$\frac{dT}{d\nu} = \frac{3\sqrt{3}T_0Q_L}{4\nu_{i,j,k}}. \tag{4}$$

So, maximizing the critically coupled Q factor and intensity gives an advantage in sensing temperature in the fixed frequency measurement. We can determine the change in transmission with respect to temperature using

$$\frac{dT}{d\xi} = \frac{3\sqrt{3}T_0Q_L}{4\nu_{i,j,k}} \times \frac{d\nu}{d\xi}, \tag{5}$$

where $d\nu/d\xi$ is the temperature dependent resonance shift equal to $-2.93(0.01)$ GHz/K. The calculation of this value will be discussed in Sec. III C. Assuming that $T_0 = 1$ we can calculate $dT/d\xi$ to be $-2.74(0.12)\,\mathrm{K}^{-1}$ using $Q_L = 136(3) \times 10^3$. This equation shows that $dT/d\xi$ scales linearly with the loaded quality factor, provided the resonator remains critically coupled and the laser spectrum is much narrower than the resonance.

C. Frequency scanning MDR thermometry

Shifts in MDR resonance frequencies, $\Delta\nu_{i,j,k}$, induced by a temperature change, $\Delta\xi$, are described by[22,32]

$$\frac{\Delta\nu_{i,j,k}}{\Delta\xi} \sim \frac{dn_{\mathrm{eff}}}{d\xi} \times \frac{\nu_{i,j,k}}{n_g}, \tag{6}$$

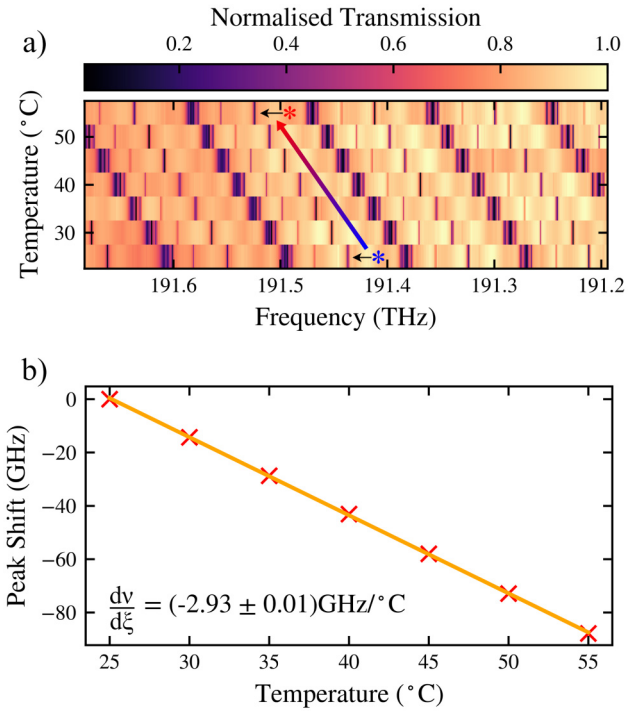

FIG. 4. (a) Temperature dependent transmission spectra of an MDR with a coupling gap of 150 nm. (b) Resonance frequency as a function of temperature of the $TE_{0,0,k}$ resonances marked with an asterisk in panel (a).

where n_{eff} and n_g are the effective mode and group index, respectively, and $dn_{\mathrm{eff}}/d\xi$ is the thermo-optic coefficient. The influence of thermal expansion on the cavity length is negligible since the thermal expansion coefficient[33] of AlN, α, is $5.8 \times 10^{-6}\,\mathrm{K}^{-1}$. For AlN, the thermo-optic coefficient[34] is $1.0 \times 10^{-5}\,\mathrm{K}^{-1}$ at 1550 nm. For comparison, Si_3N_4, SiO_2 and Si have thermo-optic coefficients of 2.45×10^{-5}, 0.95×10^{-5}, and $1.8 \times 10^{-4}\,\mathrm{K}^{-1}$ at room temperature and 1550 nm.[35–37]

To determine the accuracy with which a 1 K temperature shift can be measured, we follow the analysis of Smith *et al.*[22] The analysis assumes that (i) the temperature dependent resonance shift can be independently calibrated, (ii) the resonant frequencies of the spectrum can be determined with a least-squares fit, subject to a random standard error below the resonance's width, (iii) the standard errors on the resonant frequencies are uncorrelated (i.e., random not systematic), (iv) the linewidth of the laser (<100 kHz over 3.5 μs for the laser used here) is below that of the resonance, (v) the laser's frequency is independently calibrated and stable over the timescale of the measurement. For calibration of our device, a thermoelectric cooler (TEC) stage was used to control the temperature from 25 to 55 °C. Figure 4(a) shows the transmission spectrum as a function of temperature. Figure 4(b) shows the tracking and linear fitting of the $TE_{0,0,k}$ resonance marked by an asterisk in Fig. 4(a). The temperature dependant resonance shift, $d\nu/d\xi$, was found to be $-2.93(0.01)$ GHz/K, where the error arises from a

least-squares fit to the linear shift in frequency over this temperature range. The sign of the gradient indicates a redshift as temperature increases. Therefore, by measuring the frequency shift of a single resonance, one can determine a temperature shift equal to

$$\Delta\xi = \Delta\nu \frac{d\xi}{d\nu}. \tag{7}$$

The measured frequency shift ($\Delta\nu = \nu_2 - \nu_1$) will be determined by independent frequency measurements whose errors add in quadrature to give the uncertainty in the frequency shift, $\sigma(\Delta\nu)$. To find the uncertainty in the temperature shift, $\sigma(\Delta\xi)$, a propagation of uncertainties is followed, yielding

$$\sigma(\Delta\xi) = \Delta\xi \sqrt{\left(\frac{\sigma(\Delta\nu)}{\Delta\nu}\right)^2 + \left(\frac{\sigma(m)}{m}\right)^2}, \tag{8}$$

where $m = d\xi/d\nu$. Through this analysis, for a 1 K change in temperature, an uncertainty $\sigma(\Delta\xi) = 5.1$ mK is found. Although measured from a non-optimized device, and subject to the caveats stated above, estimated accuracy value better the performance of SPRTs and other photonic thermometers[22] (Klimov *et al.* present a photonic crystal cavity-based thermometer achieving measurement uncertainties of 175 mK,[26] Dedyulin *et al.* present MRR-based thermometers with temperature uncertainties of 10 mK[38]).

Considering N $TE_{0,0,k}$ resonances observable in Fig. 4(a), with the assumption that they all shift in an identical manner and are subject to independent measurement errors, the uncertainty on the frequency shift can be reduced to[22]

$$\sigma_N(\Delta\nu) = \frac{\sigma(\Delta\nu)}{\sqrt{N}}. \tag{9}$$

By averaging over 10 $TE_{0,0,k}$ resonances, the uncertainty in the frequency shift can be reduced to a point where the uncertainty in temperature shift is 3.6 mK, dominated by the error $\sigma(m)$. Small relative temperature shifts could be inferred from fitting the central frequency position of the resonance, rather than observing a shift of one FWHM, or by fixed-frequency measurements, at the steepest part of the transmission spectrum, but the sensitivity is again limited by the calibration of gradient m.

IV. CONCLUSION

We have demonstrated an AlN-on-sapphire microdisk resonators. The high-quality factors of these devices allow for low experimental uncertainties, surpassing SPRTs, in externally induced resonance shifts in a compact, sub-millimeter format. The on-chip nature of these devices allows for integration into other photonic components and high scalability due to the established commercial interest in the AlN. Temperature sensing in harsh environments is assured by virtue of AlN's robust material properties. In future, the other resonances in the spectra could also be used to measure temperature, provided calibration of their gradient was performed, resulting in an even lower temperature uncertainty. Additionally, obtaining a more precise calibration will serve to improve the precision of the photonic thermometer. The primary factor that currently limits the maximum achievable thermal sensitivity of our MDRs is the Q factor, which may be improved with improvements to our fabrication process. The wide transparency range of AlN could facilitate MDRs operating in the visible, where the increased thermo-optic coefficient at $\approx$ 450 nm ($3.6 \times 10^{-5}\,K^{-1}$)[39] could lead to better uncertainty in the measurements provided the quality factor can be maintained.

ACKNOWLEDGMENTS

We wish to acknowledge the support of the Henry Royce Institute for Advanced Materials through the Industrial Collaboration Programme, funded from a grant provided by the Engineering and Physical Sciences Research Council (No. EP/X527257/1). We also acknowledge financial support provided by EPSRC via Grant Nos. EP/T017813/1 and EP/03982X/1. Device processing was carried out in the cleanroom of the ERDF-funded Institute for Compound Semiconductors (ICS) at Cardiff University.

AUTHOR DECLARATIONS

Conflict of Interest

The authors have no conflicts to disclose.

Author Contributions

D. O. Armstrong: Conceptualization (equal); Formal analysis (equal); Investigation (equal); Methodology (equal); Software (equal); Writing – review & editing (equal). **J. K. Cannon:** Conceptualization (equal); Data curation (equal); Formal analysis (equal); Methodology (equal); Visualization (equal); Writing – original draft (equal). **O. Kiely:** Visualization (equal); Writing – review & editing (equal). **S. Ibrahim:** Writing – review & editing (equal). **H. B. Yağcı:** Writing – review & editing (equal). **T. Peach:** Conceptualization (equal); Resources (equal); Writing – review & editing (equal). **P. Wong:** Writing – review & editing (equal). **J. P. Hadden:** Conceptualization (equal); Resources (equal); Supervision (equal); Writing – review & editing (equal). **A. J. Bennett:** Conceptualization (equal); Formal analysis (equal); Supervision (equal); Visualization (equal); Writing – review & editing (equal).

DATA AVAILABILITY

The data that support the findings of this study are available in the Cardiff University Research Portal at https://doi.org/10.17035/cardiff.28705298.v1, Ref. 40.

REFERENCES

[1]H. Yamashita, K. Fukui, S. Misawa, and S. Yoshida, "Optical properties of aln epitaxial thin films in the vacuum ultraviolet region," J. Appl. Phys. **50**, 896–898 (1979).
[2]N. Li, C. P. Ho, S. Zhu, Y. H. Fu, Y. Zhu, and L. Y. T. Lee, "Aluminium nitride integrated photonics: A review," Nanophotonics **10**, 2347–2387 (2021).
[3]X. Liu, A. W. Bruch, and H. X. Tang, "Aluminum nitride photonic integrated circuits: From piezo-optomechanics to nonlinear optics," Adv. Opt. Photon. **15**, 236–317 (2023).

[4]W. H. P. Pernice, C. Xiong, C. Schuck, and H. X. Tang, "Second harmonic generation in phase matched aluminum nitride waveguides and micro-ring resonators," Appl. Phys. Lett. **100**, 223501 (2012).
[5]X. Guo, C.-L. Zou, and H. X. Tang, "Second-harmonic generation in aluminum nitride microrings with 2500%/w conversion efficiency," Optica **3**, 1126–1131 (2016).
[6]H. Jung and H. X. Tang, "Aluminum nitride as nonlinear optical material for on-chip frequency comb generation and frequency conversion," Nanophotonics **5**, 263–271 (2016).
[7]H. Jung, R. Stoll, X. Guo, D. Fischer, and H. X. Tang, "Green, red, and IR frequency comb line generation from single IR pump in AlN microring resonator," Optica **1**, 396–399 (2014).
[8]V. Avrutin, D. J. Silversmith, Y. Mori, F. Kawamura, Y. Kitaoka, and H. Morkoc, "Growth of bulk GaN and AlN: Progress and challenges," Proc. IEEE **98**, 1302–1315 (2010).
[9]A. Abid, R. Bensalem, and B. J. Sealy, "The thermal stability of AlN," J. Mater. Sci. **21**, 1301–1304 (1986).
[10]Y. Wang, G. Sha, C. Harlow, M. Yazbeck, and M. Khafizov, "Impact of nuclear reactor radiation on the performance of AlN/sapphire surface acoustic wave devices," Nucl. Instrum. Methods Phys. Res., Sect. B **481**, 35–41 (2020).
[11]D. A. Parks and B. R. Tittmann, "Radiation tolerance of piezoelectric bulk single-crystal aluminum nitride," IEEE Trans. Ultrason. Ferroelectr. Freq. Control **61**, 1216–1222 (2014).
[12]D. Yu, M. Humar, K. Meserve, R. C. Bailey, S. N. Chormaic, and F. Vollmer, "Whispering-gallery-mode sensors for biological and physical sensing," Nat. Rev. Methods Primers **1**, 83 (2021).
[13]S. Yang, Y. Wang, and H. Sun, "Advances and prospects for whispering gallery mode microcavities," Adv. Opt. Mater. **3**, 1136–1162 (2015).
[14]M. R. Foreman, J. D. Swaim, and F. Vollmer, "Whispering gallery mode sensors," Adv. Opt. Photon. **7**, 168–240 (2015).
[15]X. Jiang, A. J. Qavi, S. H. Huang, and L. Yang, "Whispering-gallery sensors," Matter **3**, 371–392 (2020).
[16]J. Su, "Label-free biological and chemical sensing using whispering gallery mode optical resonators: Past, present, and future," Sensors **17**, 540 (2017).
[17]S. Janz, S. Dedyulin, D. X. Xu, M. Vachon, S. Wang, R. Cheriton, and J. Weber, "Measurement accuracy in silicon photonic ring resonator thermometers: Identifying and mitigating intrinsic impairments," Opt. Express **32**, 551–575 (2024).
[18]S. Dedyulin, A. Todd, S. Janz, D.-X. Xu, S. Wang, M. Vachon, and J. Weber, "Packaging and precision testing of fiber-bragg-grating and silicon ring-resonator thermometers: Current status and challenges," Meas. Sci. Technol. **31**, 074002 (2020).
[19]R. Eisermann, S. Krenek, G. Winzer, and S. Rudtsch, "Photonic contact thermometry using silicon ring resonators and tuneable laser-based spectroscopy," Tech. Mess. **88**, 640–654 (2021).
[20]C. Zhang, G.-G. Kang, J. Wang, S. Wan, C.-H. Dong, Y.-J. Pan, and J.-F. Qu, "Photonic thermometer by silicon nitride microring resonator with milli-kelvin self-heating effect," Measurement **188**, 110494 (2022).
[21]J. Wang, C. Zhang, J. Gao, S. Wan, C. Dong, Y. Shen, Y. Pan, Q. Han, K. Zhou, and J. Qu, "High-resolution photonic temperature measurement system based on frequency locking of microring resonator," IEEE Trans. Instrum. Meas. **72**, 1–5 (2023).
[22]J. A. Smith, P. Hill, C. Klitis, L. Weituschat, P. A. Postigo, M. Sorel, M. D. Dawson, and M. J. Strain, "High precision integrated photonic thermometry enabled by a transfer printed diamond resonator on GaN waveguide chip," Opt. Express **29**, 29095–29106 (2021).
[23]L. Crovini, A. Actis, G. Coggiola, and A. Mangano, "Accurate thermometry by means of industrial platinum resistance thermometers," Measurement **10**, 31–38 (1992).
[24]F. L. McCrackin and S. S. Chang, "Simple calibration procedures for platinum resistance thermometers from 2.5 to 14 K," Rev. Sci. Instrum. **46**, 550–553 (1975).
[25]Z. Ahmed, N. Klimov, T. P. Purdy, T. Herman, K. Douglass, R. Fitzgerald, and R. Kundagrami, "Photonic thermometry: Upending 100 year-old paradigm in temperature metrology," Proc. SPIE **10923**, 109230L (2019).
[26]N. Klimov, T. Purdy, and Z. Ahmed, "Towards replacing resistance thermometry with photonic thermometry," Sens. Actuators, A **269**, 308–312 (2018).
[27]W. Bogaerts, P. De Heyn, T. Van Vaerenbergh, K. De Vos, S. Kumar Selvaraja, T. Claes, P. Dumon, P. Bienstman, D. Van Thourhout, and R. Baets, "Silicon microring resonators," Laser Photon. Rev. **6**, 47–73 (2012).
[28]S. Ghosh and G. Piazza, "Photonic microdisk resonators in aluminum nitride," J. Appl. Phys. **113**, 016101 (2013).
[29]X. Liu, C. Sun, B. Xiong, L. Wang, J. Wang, Y. Han, Z. Hao, H. Li, Y. Luo, J. Yan, T. Wei, Y. Zhang, and J. Wang, "Aluminum nitride-on-sapphire platform for integrated high-q microresonators," Opt. Express **25**, 587–594 (2017).
[30]B. Guha, S. Mariani, A. Lemaître, S. Combrié, G. Leo, and I. Favero, "High frequency optomechanical disk resonators in iii–v ternary semiconductors," Opt. Express **25**, 24639–24649 (2017).
[31]K. Powell, A. Shams-Ansari, S. Desai, M. Austin, J. Deng, N. Sinclair, M. Lončar, and X. Yi, "High-Q suspended optical resonators in 3C silicon carbide obtained by thermal annealing," Opt. Express **28**, 4938–4949 (2020).
[32]H. Xu, M. Hafezi, J. Fan, J. M. Taylor, G. F. Strouse, and Z. Ahmed, "Ultra-sensitive chip-based photonic temperature sensor using ring resonator structures," Opt. Express **22**, 3098–3104 (2014).
[33]S. Figge, H. Kroencke, D. Hommel, and B. Epelbaum, "Temperature dependence of the thermal expansion of ALN," Appl. Phys. Lett. **94**, 101915 (2009).
[34]A. Soltani, A. Stolz, J. Charrier, M. Mattalah, J.-C. Gerbedoen, H. A. Barkad, V. Mortet, M. Rousseau, N. Bourzgui, A. BenMoussa, and J.-C. De Jaeger, "Dispersion properties and low infrared optical losses in epitaxial aln on sapphire substrate in the visible and infrared range," J. Appl. Phys. **115**, 163515 (2014).
[35]A. Arbabi and L. L. Goddard, "Measurements of the refractive indices and thermo-optic coefficients of Si_3N_4 and SiO_x using microring resonances," Opt. Lett. **38**, 3878–3881 (2013).
[36]Y. Cui, Y. Jiang, S. Xie, X. Feng, Y. Zhang, J. Hu, and L. Jiang, "Measurement of sapphire wafer thermo-optic coefficient using high-temperature optical fiber sensors," IEEE Sens. J. **22**, 2244–2249 (2022).
[37]J. Komma, C. Schwarz, G. Hofmann, D. Heinert, and R. Nawrodt, "Thermo-optic coefficient of silicon at 1550 nm and cryogenic temperatures," Appl. Phys. Lett. **101**, 041905 (2012).
[38]S. Dedyulin, A. Grzetic-Muffo, S. Janz, D.-X. Xu, S. Wang, M. Vachon, and J. Weber, "Practical ring-resonator thermometer with an uncertainty of 10 mK," Measurement **221**, 113453 (2023).
[39]N. Watanabe, T. Kimoto, and J. Suda, "Thermo-optic coefficients of 4H-SiC, GaN, and AlN for ultraviolet to infrared regions up to 500 °C," Jpn. J. Appl. Phys. **51**, 112101 (2012).
[40]D. D. Armstrong, J. Cannon, L. Kiely, S. Ibrahim, B. Yagci, T. Peach, P. Wong, J. Hadden, and A. Bennett (2025). "Aluminium nitride on sapphire whispering gallery mode resonator data for photonic thermometry study," Dataset. https://doi.org/10.17035/cardiff.28705298